chemistry proceedings

MDPI

Proceeding Paper

The High Performance of Multi-Metal Layered Double Hydroxides (LDHs) in the Removal of Organic Dyes †

Soumaya Talbi [1,*], Amal El khanchaoui [2], Latifa Bouissane [1], Abderrafia Hafid [1], Mostafa Khouili [1], Souad Rabi [1] and Abdellatif Essoumhi [2,*]

[1] Molecular Chemistry, Materials and Catalysis Laboratory, Faculty of Sciences and Technologies, Sultan Moulay Slimane University, BP 523, Beni-Mellal 23000, Morocco; email1@email.com (L.B.); email2@email.com (A.H.); email1@email.com (M.K.); email2@email.com (S.R.)

[2] Chemicals Process and Applied Materials Laboratory, Polydisciplinary Faculty, Sultan Moulay Slimane University, BP 523, Beni-Mellal 23000, Morocco; email1@email.com

* Correspondence: soumaya.talbi@usms.ma (S.T.); a.essoumhi@gmail.com (A.E.)

† Presented at the 27th International Electronic Conference on Synthetic Organic Chemistry (ECSOC-27), 15–30 November 2023; Available online: https://ecsoc-27.sciforum.net/.

Abstract: In this work, both samples MgNiAl–LDH and MgNiFe–LDH hydrotalcites were utilized to remove the anionic dye Congo Red (CR) from an aqueous solution. Samples characterization was carried out by X-ray diffraction (XRD), infrared spectroscopy (IR) and Thermogravimetric/Differential Scanning Calorimetry (TG/DSC). Various parameters were investigated, including the initial dye concentration, adsorbent mass, contact time, solution pH, and temperature. Using classical pseudo-first-order, second-order, and intraparticle diffusion models, adsorption kinetics were investigated. The dynamical data fit well with the pseudo-second order kinetic model. The equilibrium adsorption data were analyzed using three linear adsorption models: Langmuir, Freundlich and Temkin. The findings showed that the Langmuir isotherm adequately predicts experimental results with an ideal correlation coefficient. The isothermal Langmuir model revealed a maximum adsorption capacity of q_{max} of 5548 mg/g for the MgNiFe–LDH and of 4043 mg/g for MgNiAl-LDH. This result is very useful when selecting sorbents to improve removal technology in the aquatic environment.

Keywords: layered double hydroxide; adsorption; anionic dye; Congo Red; kinetics; isotherms.

Citation: Talbi, S.; El khanchaoui, A.; Bouissane, L.; Hafid, A.; Khouili, M.; Rabi, S.; Essoumhi, A**.** The High Performance of Multi-Metal Layered Double Hydroxides (LDHs) in the Removal of Organic Dyes. **2023**, *14*, x. https://doi.org/10.3390/xxxxx

Academic Editor(s): Name

Published: 15 November 2023

1. Introduction:

The presence of organic pollutants in natural bodies of water is frequently identified, generating concerns about preserving both the environment and public health. Dyes are a complex class of organic compounds with a vast range of applications in industry and in the pharmaceutical field [1]. Large quantities of colorants are wasted, which is detrimental to natural resources [2]. Congo Red (CR) is an organic dye, in particular an anionic diazo dye, with two azo bonds. It is produced by linking bis-diazotized benzidine to two molecules of naphthenic acid [3]. CR can alter the biochemical characteristics of freshwater systems, which could have a detrimental effect on aquatic life due to its persistent chemical structure, lack of biodegradability and toxicity [4]. Furthermore, the presence of these organic pollutants can both raise chemical oxygen demand and decrease biological oxygen demand [5,6]. The development of highly effective, economical, and ecologically friendly wastewater treatment technology is therefore urgently needed. Currently, a number of physical and chemical techniques have been explored to treat contaminated water, including biodegradation [7], photocatalytic degradation [8], flocculation [9,10] and adsorption [11–13]. Pollutants are frequently separated from effluents using the adsorption technique. In particular, it is an efficient method that is inexpensive, straightforward, simple to use, and insensitive to harmful materials [14]. The adsorption process has

evaluated a wide variety of active materials, mostly to increase their adsorption capacity, lower the cost of preparation, or make them easier to use.

Due to their high anion capacity and higher surface area, layered double hydroxides (LDH) are the subject of extensive research, reusability, porosity and basic properties. Regarding low cost, high adsorption capacity and non-toxicity, they are more efficient to commercially available adsorbents [15]. LDH also known as anionic clays, represented by the general formula $[M^{II}_{1-x}M^{III}_{x}(OH)_2]$ $(A^{n-})_{x/n}.mH_2O$, where M^{2+}(Ni^{2+}, Mg^{2+}, Zn^{2+}, Mn^{2+}) and M^{3+} (Al^{3+} , Fe^{3+} , Cr^{3+} , Co^{3+}) represent the divalent and trivalent cations, respectively, and A^{n-} (OH^-, CO_3^{2-},NO_3^-, Cl^-) is a interlayer anions. The electroneutrality of the structure is guaranteed by the Columbian force of attraction between the intercalary anions and the positively charged metals on the LDH layer [16]. Layered double hydroxide is a particularly interesting substance due to the wide range of applications it has, including medication delivery, adsorbents [17], and catalysis [18]. Therefore, it would be fascinating to learn more about how LDH can be used to assess problems brought on by azo-dye pollutants. Among the many LDH species, a hydrotalcite-like substance composed of an MgAl–, MgFe-, NiAl–, NiFe-LDH using carbonates as the interlayer anions, is frequently employed for a number of applications [19–21]. In this work, three precursor cations were employed to prepare the LDHs. The redox and acid-base qualities of LDHs are improved by the isomorphic replacement of another metal. These characteristics play a crucial role in catalysis and adsorption. Hydrotalcites MgNiAl–LDH and MgNiFe–LDH are prepared, characterized by X-ray diffraction powder (XRD), and infrared spectroscopy (IR), Thermogravimetric/Differential Scanning Calorimetry (TG/DSC), then used in adsorption of Congo Red (CR).

2. Materials and Methods

Magnesium Nitrate Hexahydrate $Mg(NO_3)_2{\cdot}6H_2O$ (≥99.9%), Nickel Nitrate Hexahydrate $Ni(NO_3)_2{\cdot}6H_20$ (≥98.5%), Aluminium nitrate nonahydrate $Al(NO_3)_3{\cdot}9H_2O$ (≥99.99%), Ferric nitrate nonahydrate $Fe(NO_3)_3{\cdot}9H_2O$ (≥99.95%), and Congo Red ($C_{32}H_{22}N_6Na_2O_6S_2$) (>99%) were purchased from Sigma-Aldrich company. All products were used without further purification.

2.1. Preparation of MgNiAl and MgNiFe-LDH

MgNiAl-LDH with $(Mg^{2+} + Ni^{2+})/Al^{3+}$ molar ratios of 2 was prepared by Co-precipitation method at a constant pH. An aqueous solution containing 0.33 M of $Mg(NO_3)_2{\cdot}6H_2O$, 0.33 M of $Ni(NO_3)_2{\cdot}6H_20$ and 0.33 M of $Al(NO_3)_3{\cdot}9H_2O$ was dissolved in 75 mL distilled water. A mixed base solution (1 M NaOH and 0.5 M Na_2CO_3) dissolved in 75 mL was added dropwise to the stirred mixture at 25 °C until the pH reached 10. The resulting solution was carried out under reflux at 75 °C for 24 h. Afterward, the solution was washed several times with distilled water, filtered and dried overnight at 60 °C. Finely LDH powder was obtained [22]. Similarly, pristine MgNiFe-LDH was prepared via the identical Co-precipitation method.

2.2. Characterizations

XRD patterns at room temperature of as-prepared samples were collected in the range of $0 < 2\theta < 80°$ using X-Ray diffractometer (Bruker, D8-Advance) with Cu k_α (λ = 0.15406 nm) radiation operating with 40 mA and 40 KV. The FTIR spectra were recorded from 4000 to 400 cm^{-1} using JASCO 4600 FT/IR Spectrometer. TG–DSC curves of as-prepared samples were performed by Thermo-gravimetric analyzer (LABSYS evo SETARAM) under air atmosphere with a heating rate of 10 °C/min from room temperature to 900 °C.

The surface charge of the samples was determined by measuring the pH of zero point charge (pH_{ZPC}). An amount of 20 mg of the adsorbent was added to 20 mL of NaCl solution (0.1 M) by using HCl (0.1 M) and/or NaOH solution (0.1 M). The initial pH value was

adjusted between 2 and 12, and the conical flasks with the prepared solution were agitated on a shaker at 150 rpm for 24 h. The final pH (pH_f) values of solutions were then measured using a pH meter (pHenomenal® pH lab set pH 1000 L).

2.3. Kinetic Studies

In this experiment, a solution with a concentration of 1 g/L was prepared by dissolving the appropriate amount of CR in distilled water. After that, the solution was diluted to the required strength (50 and 100 mg/L).

Adsorption kinetics were achieved at room temperature with a contact period varying from 2 to 120 min by adding 20 mg of adsorbent in varied dye concentrations (50 and 100 mg/L).

The following equations were used to compute the amount of CR adsorbed onto LDH:

$$Q_t = \frac{C_o - C_t}{m}.V \quad (1)$$

where q_t is the amount of adsorbed CR at time t (mg/g); C_0 and C_t are the starting and at time t CR concentrations, respectively (mg/L); V(L) is the volume of the solution and m is the mass of adsorbent (g).

2.4. Adsorption Isotherms

Adsorption isotherm studies of CR were performed by adding 20 mg of adsorbent to a 25 mL batch of CR (20–350 mg/L) prepared from stock solution (500 mg/L) at deferential temperatures (298–317 K). Then, the solution was stirred for 30 min and then analyzed by a UV-vis spectrophotometer (JASCO V-730 Double Beam Spectrophotometer) at 498 nm.

The CR amount q_e and its corresponding removal efficiency R(%) at the adsorption time t(min) were respectively calculated by the following equation:

$$Q_e = \frac{C_0 - C_e}{m}.V \quad (2)$$

$$R(\%) = \frac{C_0 - C_e}{C_0}.100 \quad (3)$$

where q_e is adsorption capacity at equilibrium; C_0 and C_e (mg/L) are initial and equilibrium CR concentration respectively; m (g) is the adsorbent mass and V(L) is the volume of the solution.

3. Results and Discussion

3.1. Characterization of Prepared Samples

3.1.1. XRD Analysis

Figure 1 displays the XRD patterns of MgNiAl-LDH (Figure 1a) and MgNiFe-LDH (Figure 1b), where we can both samples exhibit numerous distinct reflections, such as double-layered hydroxide reflections, at 11.83°, 23.44°, 34.89°, 38.94°, 46.9°, and 62.5°, which correspond to (003), (006), (009), (015), (018), and (110), respectively. The distinctive diffraction peaks of both samples are sharp, fine and well symmetrical, indicating the single crystal phase and the high degree of crystallinity of the sample's crystal structure [23–25].

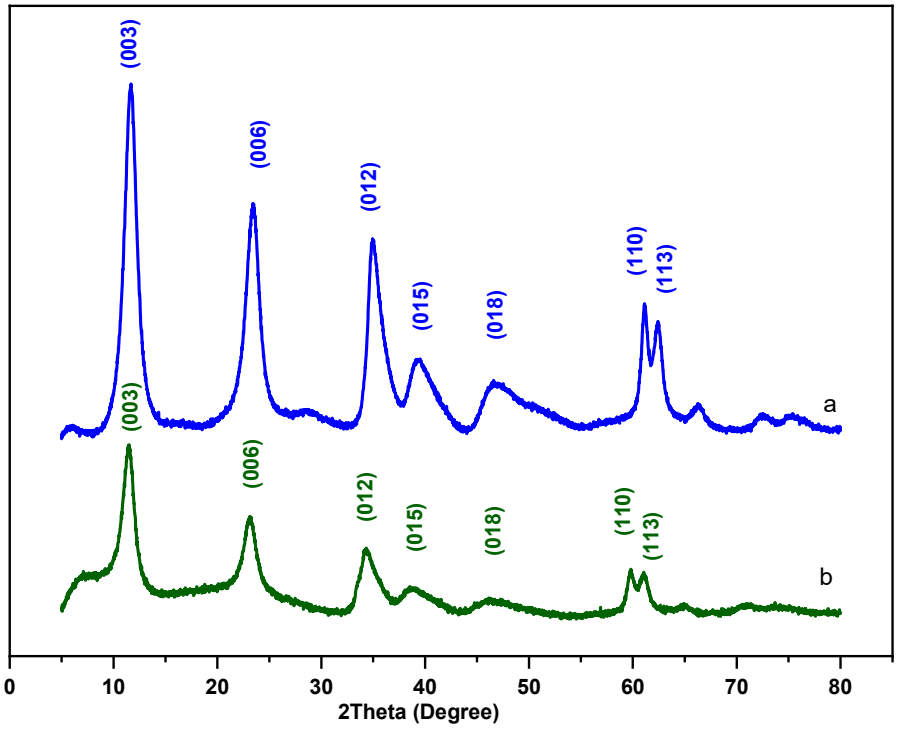

Figure 1. X-Ray pattern of (**a**) MgNiAL-LDH and (**b**) MgNiFe-LDH.

In accordance with the unit cell parameters of synthesized samples shown in Table 1, MgNiAl-LDH and MgNiFe-LDH represented 7.48 and 7.74, respectively, in the basal spacing (d003), showing that carbonate anions are located in interlayer space**.**

Table 1. Characteristic parameters of MgNiAl-LDH and MgNiFe-LDH.

Sample	**a(Å)**	**c(Å)**	**basal Spacing d_{003} (Å)**	**Interlayer Distance d(Å)**
MgNiAl-LDH	3031	22,438	7479	2679
mgnife-LDH	3093	23,225	7741	2941

3.1.2. IR Spectroscopy Analysis

The IR- spectra of the two samples MgNiAl-LDH and MgNiFe-LDH studied are presented in Figure 2, which shows that the IR spectrum of MgNiAl-LDH sample (Figure 2a), has a band located around ~ 1626 cm^{-1} (around 1630 cm^{-1} for MgNiFe LDH (Figure 2b) and the stretching vibration of the hydrogen bonding groups v(O-H) in the brucite layer and the interlayer water is represented by the very broad one at approximately 3375 cm^{-1} (around 3369 cm^{-1} for MgNiFe-LDH). The corresponding bands for intercalated carbonate anions v(CO_3^{2-}) are at 1360 and 771 cm^{-1} (1356 cm^{-1} and 711 cm^{-1} for MgNiFe-LDH). Additional adsorption bands at 616 and 558 cm^{-1} have been attributed to metal-oxygen vibrations in the layers of brucite [26].

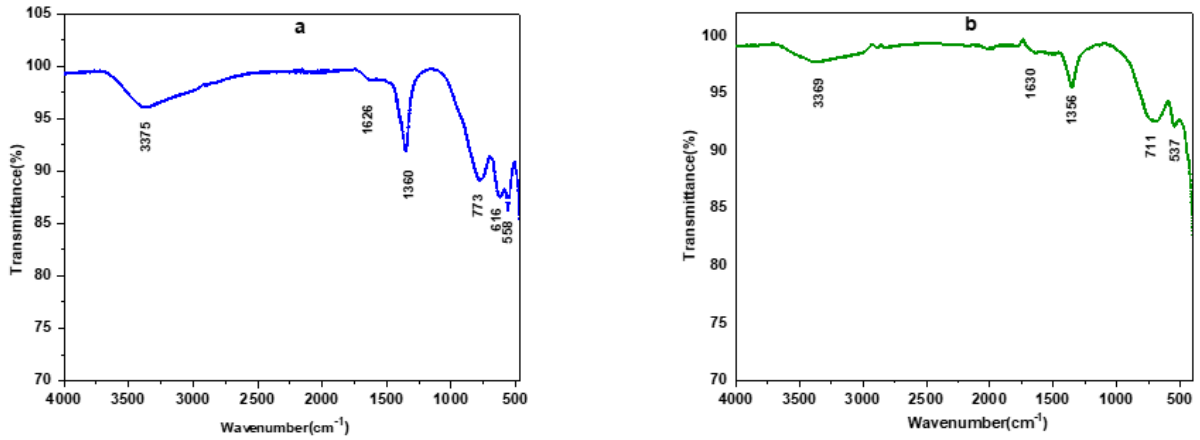

Figure 2. IR Spectra of (**a**) MgNiAl-LDH and (**b**) MgNiFe-LDH.

3.1.3. TG-DSC

The thermal decomposition of the generated materials has been studied using TG-DSC. The results are shown in Figure 3, which illustrate that the thermal degradation of the MgNiAl-LDH sample occurs, in accordance with the dTG curves, in three main steps: dehydration, dehydroxylation, and departure of the carbonate anion. Between ambient and 194 °C, dehydration occurs; this step can be explained by the detachment of interlayer water and adsorbed water. The second loss occurs in the 194–293 °C temperature range, when hydroxyl ions are removed from the brucite sheet. The interlayer carbonate thermally decomposes in the final step stage, which is completed at 640 °C. The total mass loss is 40.64% (Figure 3a). On the other hand, the thermal decomposition of the MgNiFe-LDH sample is similar to MgNiAl-LDH with a total mass loss of 33.04% (Figure 3b), a first mass loss occurred between ambient and 215 °C, the second mass loss, observed between 215 and 260 °C, and a last loss that ends at 600 °C.

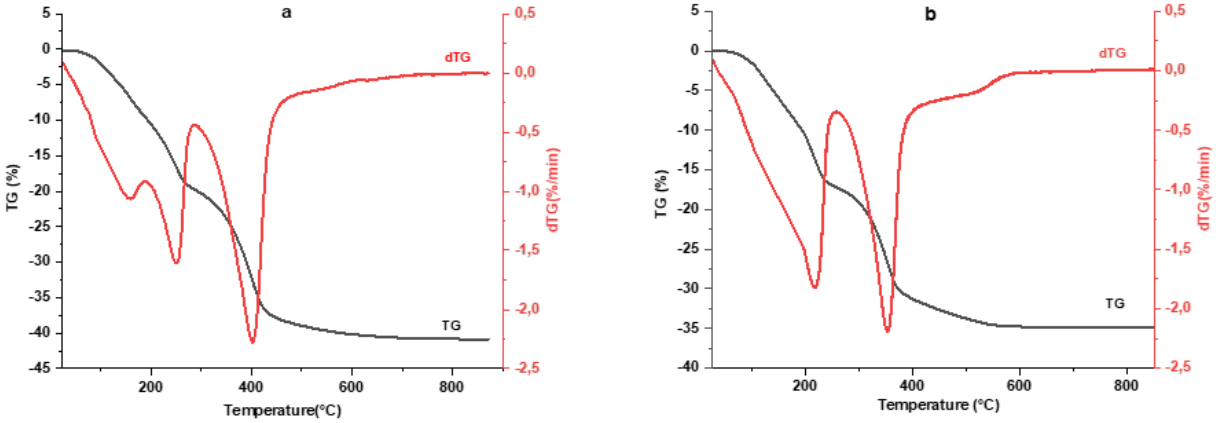

Figure 3. TG-DSC curve of (**a**) MgNiAl-LDH and (**b**) MgNiFe-LDH.

3.2. Kinetic Studies

3.2.1. pH_{pzc}

The point of zero charge (pH_{PZC}) is the parameter that corresponds to the pH at which the solid surface has zero charge (the positive charges are equal to the negative charges) [27]. Theoretically, the surface becomes positively charged at $pH < pH_{PZC}$, which facilitates the adsorption of negatively charged dye anions by electrostatic attraction forces. The surface of LDH particles becomes negatively charged when $pH > pH_{PZC}$, favoring adsorption of the cationic dye [28].

Figure 4 displays the pH_{PZC} of the two samples; MgNiAl-LDH has a pH_{PZC} of 9 (Figure 4a), whereas MgNiFe-LDH has a pH_{PZC} of 10 (Figure 4b). Below the pH_{PZC} zero charge point, the adsorbed amount of CR in LDH increases as a result of the electrostatic attraction between the positively charged adsorbent and the negative dye molecules [29]. At pH > pH_{PZC}, the adsorption capacity of LDH decreases due to the electrostatic repulsion between the adsorbent surface and the dye molecules [30]. As a result, pH = 3 was selected for both materials MgNiAl- and MgNiFe-LDH for the remainder of the study.

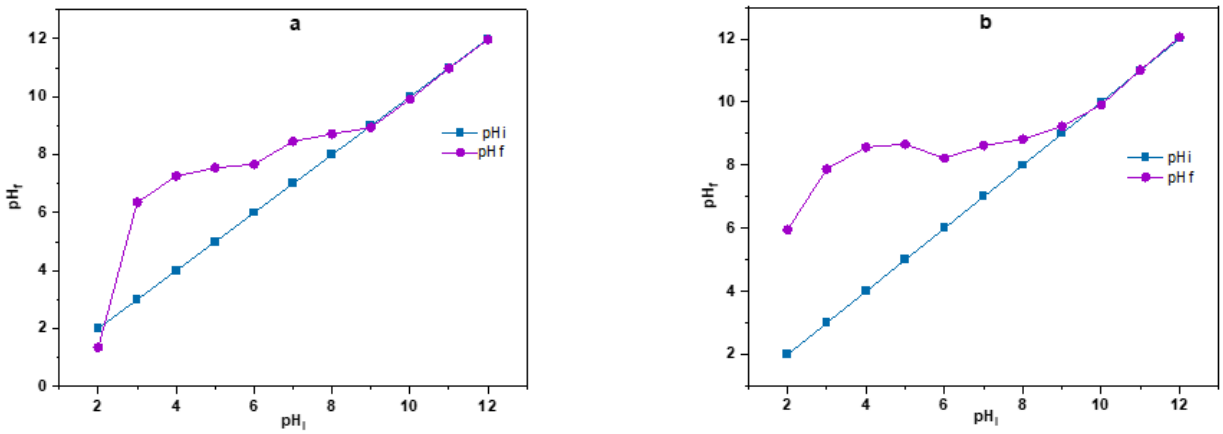

Figure 4. PZC of (**a**) MgNiAl-LDH, and (**b**) MgNiFe-LDH.

3.2.2. The Effect of Adsorbent Mass

To 25 mL of 100 mg/L CR at pH = 3, serval quantities (10–50 mg) of MgNiAl–LDH (or MgNiFe–LDH) were added. The solution was then agitated for 24 h at room temperature before being UV-vis analyzed (Figure 5).

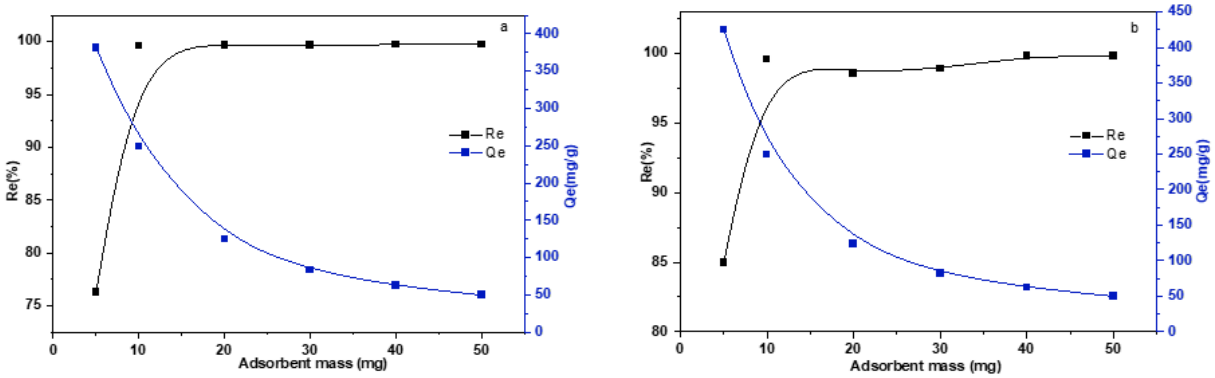

Figure 5. Effect of adsorbent mass in the adsorption of CR on (**a**) MgNiAl–LDH and (**b**) MgNiFe-LDH. (Vsol = 25 mL; CR dye concentration: 100 mg/L, temperature: 25 °C).

Figure 5 displays that the mass of LDH significantly influences the removal of CR. For the MgNiAl-LDH, the percentage of CR removal increases from 76.31 to 99.59% (Figure 5a) and from 84.99 to 99.83% for MgNiFe-LDH (Figure 5b) when the mass of adsorbent increases from 10 to 50 mg. It is remarkable that a mass of 10 mg of the LDH is able to remove a maximum of CR dye in the order of 99% for the both LDH, which indicate the speed and efficiency of LDH as a potential adsorbent for CR removal. Furthermore, this effect may be due to the low mass of the adsorbent, which causes the LDH granules to disperse in the aqueous solution, exposing all the different types of surface sites and making them accessible to CR molecules at different sites. In this case, surface adsorption is rapidly saturated, with a high adsorption capacity of up to 381.6 mg/g for MgNiAl-LDH

and to 424.95 mg/g for MgNiFe-LDH. Additionally, a large adsorbent quantity increases the probability of collision between solid particles and thus creates particle aggregation, leading to a decrease in total surface area and an increase in diffusion path length [31].

3.2.3. Effect of Contact Time on CR Adsorption

The adsorption times ranged from 0 to 120 min in order to demonstrate the impact of the contact time on the CR adsorption by the LDH samples (Figure 6). From the results obtained, we can see that the process of retention of CR by LDH is influenced by the initial concentration of dye as well as by the contact time. Figure 6 shows that the amounts of CR adsorbed increase rapidly during the first 5 min for both samples, after this time, the adsorption of dyes is almost at its maximum value corresponding to the equilibrium time (60 min) [32]. Furthermore, the exterior carbonate ions are relatively weakly attached to the particle surface and are easily replaced by CR anions, which is why the adsorption of CR anions on LDH occurs exclusively on the external surfaces of LDH particles. Furthermore, for MgNiAl-LDH the adsorption capacity increases from 62.3 to 123.65 mg/g (Figure 6a) and from 62.2 to 121.33 mg/g for MgNiFe-LDH (Figure 6b) when the initial CR dye concentration increases from 50 to 100 mg/L.

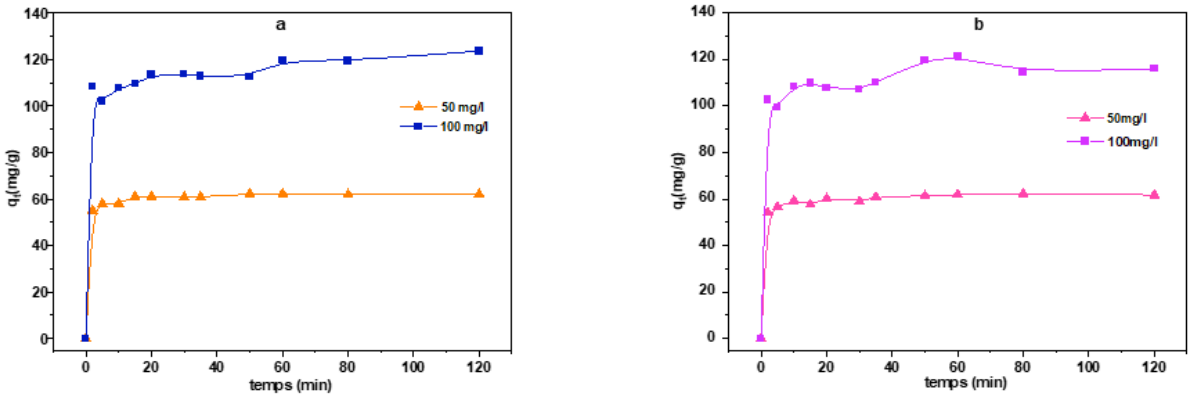

Figure 6. Time and initial concentration's effects on the adsorption of CR on (**a**) MgNiAl-LDH and (**b**) MgNiFe-LDH (V_{sol} = 20 mL; adsorbent mass = 20 mg; T = 25 °C, pH = 3).

3.2.4. Kinetic Models Applied to the Adsorption of CR onto LDHs

In order to better understand the phenomenon of dye adsorption on LDH, three kinetic models were used to evaluate the experimental results in kinetics: pseud-first order expressed by (Equation (3)) [33], pseudo-second order expressed by (Equation (4)) [34] and intra-particle diffusion model expressed by (Equation (5)) [35].

Pseudo-first-order kinetic model

$$Ln(Q_e - Q_t) = Ln(Q_e) - \frac{K_1 t}{2.303} \quad (4)$$

Pseudo-second-order kinetic model

$$\frac{t}{Q_t} = \frac{1}{K_2 Q_e^2} + \frac{t}{Q_e} \quad (5)$$

Intraparticle diffusion model

$$Q_t = K_{ip} t^{1/2} + C \quad (6)$$

where k_1 (min^{-1}), k_2 ($(g.mg^{-1}\cdot min^{-1}$ and K_{ip} ($(mg/g.\ min^{1/2})$ represents the rate constants of pseudo-first order, pseudo-second order and intra-particle diffusion kinetic models, respectively, and C the thickness of the boundary layer.

Figure 7 displays the linearized plots of Pseudo-first order, pseudo-second order, and intra particle diffusion kinetic models of CR adsorption on MgNiAl-LDH and MgNiFe-LDH, in addition, the kinetic parameters for these models are shown in Table 2, Comparing the correlation coefficient R^2 of these three models for the two samples, the pseudo-second-order model is more consistent with the results of this adsorption experiment than the pseudo-first-order model and the intra-particle diffusion model. The higher rate constant k^2 of MgNiAl-LDH (Figure 7a) obtained by the pseudo-second-order model indicates that the adsorption rate of MgNiAl-LDH is higher than that of MgNiFe-LDH (Figure 7b), which is consistent with the analysis of the adsorption kinetics. In addition, the equilibrium adsorption amount ($qe_{,cal}$: 115.47 mg/g for MgNiAl-LDH; 113.79 mg/g for MgNiFe-LDH) calculated by the pseudo-second order model is closer to the experimental value ($qe_{,exp}$: 123.65 mg/g for MgNiAl-LDH; 121.33 mg/g for MgNiFe-LDH). Therefore, utilizing pseudo-second order kinetics to describe the adsorption of CR on the surface of both samples is more accurate.

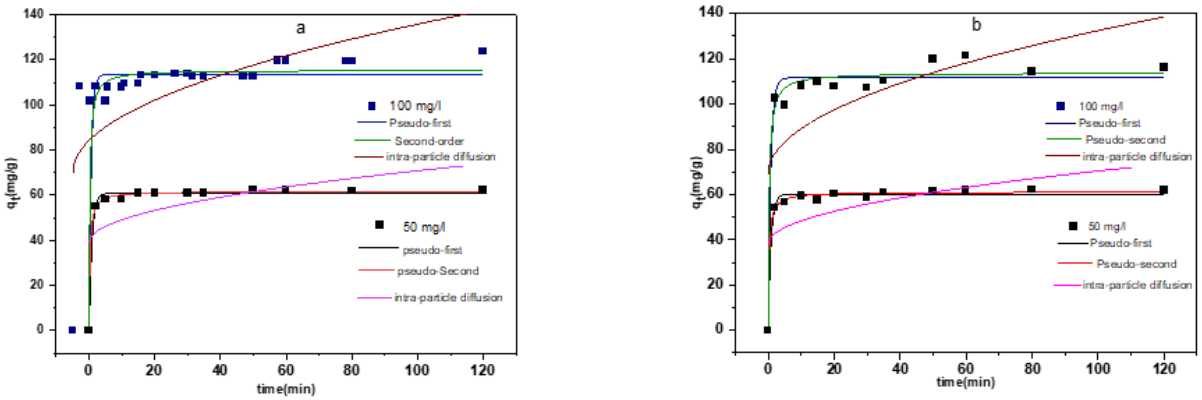

Figure 7. CR adsorption kinetic model with pseudo-first order, pseudo-second order, and intra-particle diffusion onto (**a**) MgNiAl-LDH and (**b**) onto MgNiFe-LDH.

Table 2. The parameters of the CR adsorption kinetic model on MgNiAl-LDH and MgNiFe-LDH pseudo-first-order, pseudo-second-order and intra-particle diffusion.

C_0	$q_{e,exp}$	Pseudo-First Order			Pseudo-Second Order			Intra-Particle Diffusion		
		$q_{e,cal}$	k_1	R^2	$q_{e,cal}$	k_2	R^2	K_{ip}	C	R^2
MgNiAl-LDH										
50	62,287	60,890	1,158	0,993	61,791	0,059	0,997	3,179	39,069	0,340
100	123,650	113,477	1,508	0,998	115,477	0,035	0,978	6,522	70,254	0,400
MgNiFe-LDH										
50	62,220	60,168	1,139	0,990	61,129	0,056	0,995	3,225	38,159	0,357
100	121,330	111,526	1,225	0,967	111,798	0,027	0,978	6,342	69,029	0,393

Furthermore, the intra-particle diffusion kinetic model plot for both MgNiAl-LDH (Figure 7a) and MgNiFe-LDH Figure 7b) materials clearly reveals the existence of serval steps during the adsorption process. In accord with this model, if the linear plot passes through the origin, intraparticle diffusion controls the rate of adsorption kinetics. However, Figure 7 clearly shows that the plot does not pass through the origin, indicating that the adsorption process involves intraparticle diffusion, which is not the only rate-limiting step [36]. The first step is the adsorption on a readily available outside adsorption site, the middle step is the diffusion of dye molecules within the pores, and the last step is the equilibrium process, where complete adsorption on the unoccupied sites has been

achieved [37]. Surface adsorption and intraparticle diffusion are both confirmed by the plot. Furthermore, the thickness of the boundary layer C increases with increasing CR dye concentration (50 and 100 mg/L), it can be accounted for by an increase in boundary layer effect brought on by the instantaneous adsorption of accessible sites [16].

3.3. Adsorption Isotherms

Adsorption isotherms, for solid-liquid systems, are among the important physicochemical aspects, they allow to show the adsorbent-adsorbate affinity, to understand some mechanisms related to adsorption and also to know the maximum quantity that an adsorbent can retain on its surface [38]. In this study, three well-known Langmuir, Freundlich and Temkin isotherm models are assessed. The parameters collected from the various models offer crucial details on the sorption mechanisms as well as the sorbent's surface characteristics and affinities.

Langmuir's adsorption model is based on the principle that a saturated monolayer of solute molecules on the adsorbent surface is equivalent to maximum adsorption. As a result, the Langmuir isotherm model was chosen to calculate the maximal adsorption capacity q_m, which equates to complete monolayer coverage on the sorbent surface. The following is the supplied equation [39,40]:

$$\frac{C_e}{Q_e} = \frac{1}{Q_m} C_e + \frac{1}{Q_m K} \quad (7)$$

K_L is Langmuir's constant and relates to the adsorption energy. The value of K_L indicates whether the isotherm is unfavorable ($K_L > 1$), linear ($K_L = 1$), favorable ($0 < K_L < 1$) or irreversible ($K_L = 0$).

Freundlich theory suggests multilayer adsorption, which takes place on a heterogeneous surface containing sites with different adsorption energies. The maximum adsorption occurs when the surface is covered with a monolayer of adsorbent [41]. The Freundlich equation can be described as shown below [42]:

$$Ln(Q_e) = Ln(K_F) + \frac{1}{n} Ln(C_e) \quad (8)$$

In terms of adsorption capacity, K_F is the Freundlich isotherm constant (L/g), and 1/n is the heterogeneity factor.

The Temkin isotherm model [43] describes the interaction adsorbate-adsorbent on an adsorption isotherm. The Temkin isotherm model can be stated as follows:

$$Q_e = \frac{RT}{b_T} Ln(K_T) + \frac{RT}{b_T} Ln(C_e) \quad (9)$$

where K_T is the Temkin isotherm constant (L/g), R is the gas constant (8.314 J /mol.K), T is the absolute temperature (K) and B = RT/b, b is the Temkin constant related to the heat of adsorption (J/mol).

The isotherm data obtained at 298 K were fitted according to the Langmuir, Freundlich and Temkin models for MgNiAl-LDH and MgNiFe-LDH, as shown in Figure 8. The isothermal parameters of all models are summarized in Table 3. From the results obtained, the values of 1/n calculated at 298 K for both samples are between 0 and 1, which indicates that the CR adsorption is favorable according to what was mentioned above. However, the acceptability of the isothermal model that best fits the experimental data is determined on the basis of the correlation coefficient R^2 value closest to unity. The Langmuir isotherm is based on the adsorption of a homogenous monolayer adsorbent material with uniform energy at all active adsorption sites. The Freundlich isotherm involves multilayer and heterogenous adsorption of adsorbent molecules on the sorbent surface, in contrast to the Langmuir model. Adsorption isotherms were analyzed for MgNiAl-LDH and MgNiFe-

LDH, it indicated that for both samples, the R^2 value of the Langmuir isotherm was better than that of the Freundlich and Temkin isotherm. As a result, the adsorption of CR occurred in the monolayer on the surface of both LDH and its maximum adsorption capacity was found to be 5584 mg/g for MgNiFe-LDH (Figure 8a) and 4043 mg/g for MgNiAl-LDH (Figure 8b).

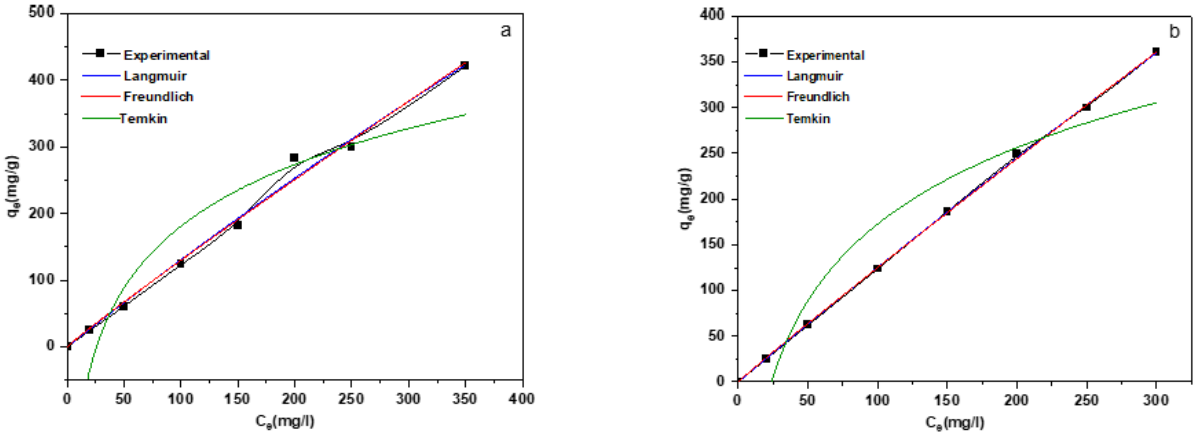

Figure 8. Adsorption isotherms and model plots for the adsorption of CR onto (**a**) MgNiAl-LDH and (**b**) MgNiFe-LDH.

Table 3. Parameter values for Langmuir, Freundlich and Temkin adsorption isotherm models for CR adsorption onto MgNiAl-LDH and MgNiFe-LDH (Adsorbent = 20 mg, CR= 25 mL of 20–350 mg/L, T = 298 K).

Temperature	Langmuir			Freundlich			Temkin		
(K)	q_m	k_L	R^2	K_F	1/n	R^2	K_T	B	R^2
MgNiAl-LDH									
298	4043,190	3,34035 × 10^{-4}	0,991	1,638	1,053	0,988	0,038	133,436	0,899
MgNiFe-LDH									
298	5584,740	2,29685 × 10^{-4}	0,969	1,471	1,036	0,999	0,041	120,778	0,919

Table 4 compares the maximal adsorption capabilities of CR adsorbents with those of other adsorbents**.** MgNiFe-LDH and MgNiAl-LDH have significantly higher CR adsorption capacity than other ratios [44–53]. As a result, due to their high adsorption capacity and simplicity of synthesis, adsorbents as created are regarded as attractive options for the disposal of dye-containing effluents.

Table 4. CR adsorption capacity of MgNiAl-LDH and MgNiFe-LDH samples and other reported adsorbents.

ADSORBENT	ADSORPTION CAPACITY (MG/G)	REFERENCE
MgNiFe-LDH	5584	This work
MgNiAl-LDH	4043	This work
MgNiCo-LDH	1194,7	[44]
ZnAl-LDH/$Al(OH)_3$	2348	[45]
Histidine/MgAl-LDH	1112	[46]
$ZnFe_2O_4$/MgAl-LDH	294	[47]
ZnAl-550	166,1	[48]

ZrO_2/MgAl-LDH	169	[49]
NiFe-LDH/Au	625	[50]
NiCo-LDH	909	[51]
Gly-LDH	800	[52]
NIFE-LDH	484	[53]

4. Conclusions

According to the study's findings, Produced LDHs are excellent anionic dye sorbents, particularly effective for removing CR dye at quite high concentrations. The pseudo-second-order kinetic model successfully fit the adsorption kinetic data, while the Langmuir model perfectly modeled the isothermal data. Using the produced LDHs, the anionic dye CR was successfully removed with an adsorption equilibrium time of 60 min and the highest adsorption capacities for MgNiAl-LDH and MgNiFe-LDH, respectively, are 4043 mg/g and 5584 mg/g. When compared to other adsorbents, we believe that the prepared materials are incredibly competitive and show great promise for the removal of anionic dyes in industrial wastewater treatment.

References

1. Benkhaya, S.; M'rabet, S.; El Harfi, A. A review on classifications, recent synthesis and applications of textile dyes. *Inorg. Chem. Commun.* **2020**, *115*, 107891. https://doi.org/10.1016/j.inoche.2020.107891.
2. Krishnamoorthy, R.; Choudhury, A.R.; Jose, P.A.; et al. Long-term exposure to azo dyes from textile wastewater causes the abundance of saccharibacteria population. *Appl. Sci.* **2021**, *11*, 379. https://doi.org/10.3390/app11010379.
3. Kalwar, N.H.; Sirajuddin Sherazi, S.T.H.; et al. Fabrication of small l-threonine capped nickel nanoparticles and their catalytic application. *Appl. Catal.* **2013**, *453*, 54–55. https://doi.org/10.1016/j.apcata.2012.12.005.
4. Carneiro, P.A.; Umbuzeiro, G.A.; Oliveira, D.P.; et al. Assessment of water contamination caused by a mutagenic textile effluent/dyehouse effluent bearing disperse dyes. *J. Hazard. Mater.* **2010**, *174*, 694–699. https://doi.org/10.1016/j.jhazmat.2009.09.106.
5. Holkar, C.R.; Jadhav, A.J.; Pinjari, D.V.; et al. A critical review on textile wastewater treatments: Possible approaches. *J. Environ. Manage.* **2016**, *182*, 351–366. https://doi.org/10.1016/j.jenvman.2016.07.090.
6. Lellis, B.; Fávaro-Polonio, C.Z.; Pamphile, J.A.; et al. Effects of textile dyes on health and the environment and bioremediation potential of living organisms. *Biotechnol. Res. Innov.* **2019**, *3*, 275–290. https://doi.org/10.1016/j.biori.2019.09.001.
7. Ghattas, A.K.; Fischer, F.; Wick, A.; et al. Anaerobic biodegradation of (emerging) organic contaminants in the aquatic environment. *Water Res.* **2017**, *116*, 268–295. https://doi.org/10.1016/j.watres.2017.02.001.
8. Aboutaleb, W.A.; El-Salamony, R.A. Effect of Fe_2O_3-CeO_2 nanocomposite synthesis method on the Congo red dye photodegradation under visible light irradiation. *Mater. Chem. Phys.* **2019**, *236*, 121724. https://doi.org/10.1016/j.matchemphys.2019.121724.
9. Huang, X.; Bo, X.; Zhao, Y.; et al. Effects of compound bioflocculant on coagulation performance and floc properties for dye removal. *Bioresour. Technol.* **2014**, *165*, 116–121. https://doi.org/10.1016/j.biortech.2014.02.125.
10. Dotto, J.; Fagundes-Klen, M.R.; Veit, M.T.; et al. Performance of different coagulants in the coagulation/flocculation process of textile wastewater. *J. Clean. Prod.* **2019**, *208*, 656–665. https://doi.org/10.1016/j.jclepro.2018.10.112.
11. Wang, Y.; Dai, X.; Zhou, Q.; et al. Insights into the role of metal cation substitution on the anionic dye removal performance of CoAl-LDH. *Colloids Surf A Physicochem.* **2022**, *636*, 128139. https://doi.org/10.1016/j.colsurfa.2021.128139.
12. Sriram, G.; Uthappa, U.T.; Losic, D.; et al. MgAl-layered double hydroxide (LDH) modified diatoms for highly efficient removal of Congo red from aqueous solution. *Appl. Sci.* **2020**, *10*, 2285. https://doi.org/10.3390/app10072285.
13. Salem, M.A.S.; Khan, A.M.; Manea, Y.K.; et al. Nano chromium embedded in f-CNT supported CoBi-LDH nanocomposites for selective adsorption of Pb2+and hazardous organic dyes. *Chemosphere* **2022**, *289*, 133073. https://doi.org/10.1016/j.chemosphere.2021.133073.
14. Taher, T.; Rohendi, D.; Mohadi, R.; et al. Congo red dye removal from aqueous solution by acid-activated bentonite from sarolangun: Kinetic, equilibrium, and thermodynamic studies. *Arab. J. Basic. Appl. Sci.* **2019**, *26*, 125–136. https://doi.org/10.1080/25765299.2019.1576274.
15. El Khanchaoui, A.; Sajieddine, M.; Mansori, M.; et al. Removal of single dye and dye mixture from aqueous solution with alginate-coated calcined layered double hydroxide and illite clay composite beads. *Mater. Res. Innov.* **2023**, *27*, 355–370. https://doi.org/10.1080/14328917.2022.2163112.
16. Brahma, D.; Saikia, H. Synthesis of ZrO_2/MgAl-LDH composites and evaluation of its isotherm, kinetics and thermodynamic properties in the adsorption of congo red dye. *J. Chem. Thermodyn.* **2022**, *7*, 100067. https://doi.org/10.1016/j.ctta.2022.100067.
17. Dib, M.; Ouchetto, H.; Akhramez, S.; et al. Preparation of Mg/Al-LDH nanomaterials and its application in the condensation of 3-Amino-1-phenyl-2-pyrazolin-5-one with aromatic aldehyde. *Mater. Today Proc.* **2020**, *22*, 104–107. https://doi.org/10.1016/j.matpr.2019.08.106.

18. Ke, G.; Tan, H.; Yang, P.; et al. Preparation and adsorption properties of rod mgnial-ldh. *Mater. Sci. Forum.* **2019**, *956*, 294–304. https://doi.org/10.4028/www.scientific.net/MSF.956.294.
19. Ai, L.; Zhang, C.; Meng, L. Adsorption of methyl orange from aqueous solution on hydrothermal synthesized Mg-Al layered double hydroxide. *J. Chem. Eng. Data* **2011**, *56*, 4217–4225. https://doi.org/10.1021/je200743u.
20. Zhong, C.; Su, S.; Xu, L.; et al. Preparation of NiAl-LDH/Polypyrrole composites for uranium (VI) extraction from simulated seawater. *Colloids Surf. A Physicochem.* **2019**, *562*, 329–335. https://doi.org/10.1016/j.colsurfa.2018.11.029.
21. Hu, H.; Wageh, S.; Al-Ghamdi, A.A. NiFeLDH nanosheet/carbon fiber nanocomposite with enhanced anionic dye adsorption performance. *Appl. Surf. Sci.* **2020**, *511*, 145570. https://doi.org/10.1016/j.apsusc.2020.145570.
22. El Khanchaoui, A.; Sajieddine, M.; Mansori, M.; et al. Anionic dye adsorption on ZnAl hydrotalcite-type and regeneration studies based on "memory effect". *J. Environ. Anal. Chem.* **2020**, *102*, 3542–3560. https://doi.org/10.1080/03067319.2020.1772769.
23. Zaghouane-Boudiaf, H.; Boutahala, M.; Arab, L. Removal of methyl orange from aqueous solution by uncalcined and calcined MgNiAl layered double hydroxides (LDHs). *J. Chem. Eng.* **2012**, *187*, 142–149. https://doi.org/10.1016/j.cej.2012.01.112.
24. Li, S.S.; Jiang, M.; Jiang, T.J.; et al. Competitive adsorption behavior toward metal ions on nano-Fe/Mg/Ni ternary layered double hydroxide proved by XPS: Evidence of selective and sensitive detection of Pb(II). *J. Hazard. Mater.* **2017**, *338*, 1–10. https://doi.org/10.1016/j.jhazmat.2017.05.017.
25. Ul Hasnain, M.A.; Khoja, A.H.; Butt, F.B.; et al. Partial oxidation of methane over CeO2 loaded hydrotalcite (MgNiAl) catalyst for the production of hydrogen rich syngas (H2, CO). *Int. J. Hydrog. Energy.* **2021**, *46*, 36663–36667. https://doi.org/10.1016/j.ijhydene.2021.08.169.
26. Lafi, R.; Charradi, K.; Djebbi, M.A.; et al. Adsorption study of Congo red dye from aqueous solution to Mg-Al-layered double hydroxide. *Adv. Powder Technol.* **2016**, *27*, 232–237. https://doi.org/10.1016/j.apt.2015.12.004.
27. Garrison, S. On Points of Zero Charge. *Environ. Sci. Technol.* **1998**, *32*, 2815–2819. https://doi.org/10.1021/es9802347.
28. Palapa, N.R.; Taher, T.; Rahayu, B.R.; et al. CuAl LDH/Rice husk biochar composite for enhanced adsorptive removal of cationic dye from aqueous solution. *Chem. React. Eng.* **2020**, *15*, 527–537. https://doi.org/10.9767/bcrec.15.2.7828.525-537.
29. Farghali, M.A.; Selim, A.M.; Khater, H.F.; et al. Optimized adsorption and effective disposal of Congo red dye from wastewater: Hydrothermal fabrication of MgAl-LDH nanohydrotalcite-like materials. *Arab. J. Chem.* **2022**, *15*, 104–171. https://doi.org/10.1016/j.arabjc.2022.104171.
30. Sonal, S.; Prakash, P.; Mishra, B.K.; et al. Synthesis, characterization and sorption studies of a zirconium (IV) impregnated highly functionalized mesoporous actIVated carbonsb. *RSC Adv.* **2020**, *10*, 13783–13798. https://doi.org/10.1039/c9ra10103a.
31. Shabbir, R.; Gu, A.; Chen, J.; et al. Highly efficient removal of congo red and methyl orange by using petal-like Fe-Mg layered double hydroxide. *J. Environ. Anal. Chem.* **2020**, *102*, 1060–1077. https://doi.org/10.1080/03067319.2020.1730343.
32. Munir, M.; Nazar, M.F.; Zafar, M.N.; et al. Effective Adsorptive Removal of Methylene Blue from Water by Didodecyldimethylammonium Bromide-Modified Brown Clay. *ACS Omega* **2020**, *5*, 16711–16721. https://doi.org/10.1021/acsomega.0c01613.
33. Feng, Z.; Shao, Z.; Yao, J.; et al. Protein adsorption and separation with chitosan-based amphoteric membranes. *Polym. J.* **2009**, *50*, 1257–1263. https://doi.org/10.1016/j.polymer.2008.12.046.
34. Ho, Y.S.; Ofomaja, A.E. Pseudo-second-order model for lead ion sorption from aqueous solutions onto palm kernel fiber. *J. Hazard. Mater.* **2006**, *129*, 137–142. https://doi.org/10.1016/j.jhazmat.2005.08.020.
35. Wu, F.C.; Tseng, R.L.; Juang, R.S. Initial behavior of intraparticle diffusion model used in the description of adsorption kinetics. *J. Chem. Eng.* **2009**, *153*, 1–8. https://doi.org/10.1016/j.cej.2009.04.042.
36. Doğan, M.; Abak, H.; Alkan, M. Adsorption of methylene blue onto hazelnut shell: Kinetics, mechanism and activation parameters. *J. Hazard. Mater.* **2009**, *164*, 172–181. https://doi.org/10.1016/j.jhazmat.2008.07.155.
37. Kostić, M.; Najdanović, S.; Velinov, N.; et al. Ultrasound-assisted synthesis of a new material based on MgCoAl-LDH: Characterization and optimization of sorption for progressive treatment of water Environ. *Technol. Innov.* **2022**, *26*, 102358. https://doi.org/10.1016/j.eti.2022.102358.
38. Senthil Kumar, P.; Ramalingam, S.; Senthamarai, C. Adsorption of dye from aqueous solution by cashew nut shell: Studies on equilibrium isotherm, kinetics and thermodynamics of interactions. *Desalination* **2010**, *261*, 52–60. https://doi.org/10.1016/j.desal.2010.05.032.
39. Almoisheer, N.; Alseroury, F.A.; Kumar, R. Adsorption and anion exchange insight of indigo carmine onto CuAl-LDH/SWCNTs nanocomposite: Kinetic, thermodynamic and isotherm analysis. *RSC Adv.* **2019**, *9*, 560–568. https://doi.org/10.1039/C8RA09562K.
40. Najafi, M.; Bastami, T.R.; Binesh, N.; et al. Sono-sorption versus adsorption for the removal of congo red from aqueous solution using NiFeLDH/Au nanocomposite: Kinetics, thermodynamics, isotherm studies, and optimization of process parameters. *J. Ind. Eng. Chem.* **2022**, *116*, 489–503. https://doi.org/10.1016/j.jiec.2022.09.039.
41. Nyankson, E.; Adjasoo, J.; Efavi, J.K.; et al. Characterization and evaluation of zeolite A/Fe3O4 nanocomposite as a potential adsorbent for removal of organic molecules from wastewater. *J. Chem.* **2019**, *2019*, 8090756. https://doi.org/10.1155/2019/8090756.
42. Crini, G.; Peindy, H.N.; Gimbert, F.; et al. Removal of, C.I. Basic Green 4 (Malachite Green) from aqueous solutions by adsorption using cyclodextrin-based adsorbent: Kinetic and equilibrium studies. *Sep. Purif. Technol.* **2007**, *53*, 97–110. https://doi.org/10.1016/j.seppur.2006.06.018.
43. Khodam, F.; Rezvani, Z.; Amani-Ghadim, A.R. Enhanced adsorption of Acid Red 14 by co-assembled LDH/MWCNTs nanohybrid: Optimization, kinetic and isotherm. *J. Ind. Eng. Chem.* **2015**, *21*, 1286–1294. https://doi.org/10.1016/j.jiec.2014.06.002.

44. Wang, X.; Cheng, B.; Zhang, L.; et al. Synthesis of MgNiCo LDH hollow structure derived from ZIF-67 as superb adsorbent for Congo red. *J. Colloid. Interface Sci.* **2022**, *612*, 598–607. https://doi.org/10.1016/j.jcis.2021.12.176.
45. Guo, X.; Yin, P.; Yang, H. Superb adsorption of organic dyes from aqueous solution on hierarchically porous composites constructed by ZnAl-LDH/Al(OH)$_3$ nanosheets. *Microporous Mesoporous Mat.* **2018**, *259*, 123–133. https://doi.org/10.1016/j.micromeso.2017.10.003.
46. Shamsayei, M.; Yamini, Y.; Asiabi, H. Fabrication of zwitterionic histidine/layered double hydroxide hybrid nanosheets for highly efficient and fast removal of anionic dyes. *J. Colloid. Interface Sci.* **2018**, *529*, 255–264. https://doi.org/10.1016/j.jcis.2018.06.022.
47. Sun, Q.; Tang, M.; Hendriksen, P.V.; et al. Biotemplated fabrication of a 3D hierarchical structure of magnetic $ZnFe_2O_4$/MgAl-LDH for efficient elimination of dye from water. *J. Alloys Compd.* **2020**, *829*, 154552. https://doi.org/10.1016/j.jallcom.2020.154552.
48. El Khanchaoui, A.; Sajieddine, M.; Mansori, M.; et al. Calcined ZnAl-LDH trapping performance in alginate beads for adsorption of Congo Red dye. *J. Environ. Anal. Chem.* 2021. https://doi.org/10.1080/03067319.2021.1959565.
49. Brahma, D.; Saikia, H. Synthesis of ZrO_2/MgAl-LDH composites and evaluation of its isotherm, kinetics and thermodynamic properties in the adsorption of congo red dye. *J. Chem. Thermodyn.* **2022**, *7*, 100067. https://doi.org/10.1016/j.ctta.2022.100067.
50. Najafi, M.; Bastami, T.R.; Binesh, N.; et al. Sono-sorption versus adsorption for the removal of congo red from aqueous solution using NiFeLDH/Au nanocomposite: Kinetics, thermodynamics, isotherm studies, and optimization of process parameters. *J. Ind. Eng. Chem.* **2022**, *116*, 489–503. https://doi.org/10.1016/j.jiec.2022.09.039.
51. Hu, H.; Liu, J.; Xu, Z. Hierarchical porous Ni/Co-LDH hollow dodecahedron with excellent adsorption property for Congo red and Cr(VI) ions. *Appl. Surf. Sci.* **2019**, *478*, 981–990. https://doi.org/10.1016/j.apsusc.2019.02.008.
52. El Khanchaoui, A.; Boukontar, N.; Sajieddine, M.; et al. Noticeable improvement in adsorption capacity of glycine-modified MgAl-LDH in the removal of Methyl Orange dye compared to urea standard method. *Mater. Res. Innov.* **2022**, *27*, 152–162. https://doi.org/10.1080/14328917.2022.2101305.
53. Hu, H.; Wageh, S.; Al-Ghamdi, A.A.; et al. NiFeLDH nanosheet/carbon fiber nanocomposite with enhanced anionic dye adsorption performance. *Appl. Surf. Sci.* **2020**, *511*, 144570. https://doi.org/10.1016/j.apsusc.2020.145570.